

Universal intrinsic higher-rank spin Hall effect

Junpeng Hou,^{1,*} Ying Su,^{1,*} and Chuanwei Zhang^{1,†}

¹*Department of Physics, The University of Texas at Dallas, Richardson, Texas 75080-3021, USA*

Spin Hall effect (SHE), a fundamental transport phenomenon with non-zero spin current but vanishing charge current, has important applications in spintronics for the electrical control of spins. Owing to the half-spin nature of electrons, the rank of spin current (determined by the rank of spin tensors) has been restricted to 0 and 1 for charge and spin Hall effects. Motivated by recent studies of pseudospin-1 fermions in solid state and cold atomic systems, here we introduce and characterize higher-rank (≥ 2) SHEs in large spin (≥ 1) systems. We find a universal rank-2 spin Hall conductivity $e/8\pi$, with zero rank-0 and 1 conductivities, for a spin-1 model with intrinsic spin-orbit coupling. Similar rank-2 SHEs can also be found in a spin-3/2 system. An experimental scheme is proposed to realize and measure rank-2 SHEs with pseudospin-1 ultracold fermionic atoms. Our results reveal novel spin transport phenomena in large spin systems and may find important applications in designing innovative spintronic devices.

Introduction. Hall effects and their quantized siblings are one of the major cornerstones of modern condensed-matter physics, and the discovery of novel Hall effects often opens new avenues for controlling electronic transport for device applications. One of the most notable examples in this context is probably the spin Hall effect (SHE), where spin up and down of electrons move along opposite transverse directions under an applied electric field, yielding non-zero spin current but vanishing charge current (see Fig. 1(a) for an illustration) [1, 2]. Spin-current-based phenomena such as giant SHE [3–5], inverse SHE [6–10] and quantum SHE [11–13], have also been widely studied. SHE provides a powerful tool for controlling spins electrically, thus has significant applications for realizing low-power spintronic devices [2].

The origin of SHE can be attributed to either extrinsic impurity scattering [14] or intrinsic spin-orbit coupling (SOC) [15, 16]. In intrinsic SHE, the SOC serves as an effective magnetic field that is opposite for spin up and down, yielding nonzero spin-Hall current. For instance, in a two-dimensional (2D) electronic gas, the Rashba SOC yields a spin-Hall conductivity $e/8\pi$, which is a universal constant that does not depend on the underlying material properties [16]. Here the spin current operator is generally defined by $\mathbf{J}_s = \frac{1}{2} \{S_z, \mathbf{v}\}_+$ with $S_z = \frac{\hbar}{2} \sigma_z$ and the rank-1 Pauli matrix σ_z , where $\{\cdot, \cdot\}_+$ denotes the anticommutator and \mathbf{v} is the velocity operator. In this sense, the charge-current operator $\sigma_0 \mathbf{v}$ can be viewed as rank-0, where σ_0 is the 2×2 identity matrix. For electrons with half spin, 0 and 1 are only available ranks for spin-1/2 matrices.

Recent theoretical and experimental advances in the study of pseudospin-1 fermions have opened a new perspective towards the realization of novel quantum phases and dynamics in large-spin systems, in which higher-rank spin-tensors exist and play a crucial role [1]. In particular, triply-degenerate fermions were proposed as novel quasiparticles without counterparts in quantum field theory [18, 19] and certain experimental signatures have been observed in solid-state materials [20]. Moreover,

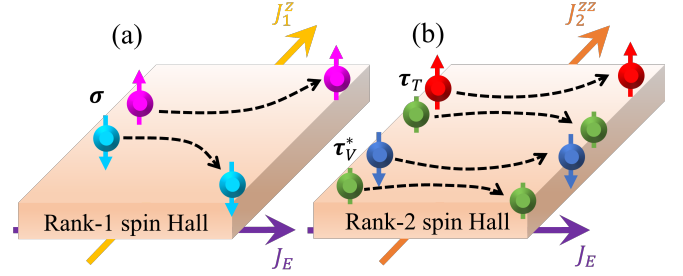


FIG. 1. Illustration of higher-rank spin-Hall effect. (a) In the rank-1 SHE of a spin-1/2 system, the spin up and down components move along opposite directions, yielding a vanishing rank-0 charge Hall current but a finite rank-1 spin Hall current \mathbf{J}_1^z . (b) Rank-2 SHE in a spin-1 fermionic system, where both charge (rank-0) and rank-1 spin currents vanish, leaving only non-zero rank-2 spin current \mathbf{J}_2^{zz} . The red, green and blue disks correspond to spin components $|m_z = 1\rangle$, $|0\rangle$ and $|-1\rangle$ respectively. In both cases, the electric field is applied along the x direction, leading to a charge current \mathbf{J}_E while transverse charge current \mathbf{J}_0 remains zero.

large-spin ($> 1/2$) is easily accessible in experiments for ultracold atoms, superconducting qubits, and trapped ions with multiple pseudospin states [21–24], which can host interesting quantum phases [25–30] and topological states [6, 31, 33–35].

While these works reveal many fascinating phenomena, spin transport in large spin systems, particularly when involve higher-rank spin tensors, remains largely unexplored. A natural question is whether there is intrinsic higher-rank (≥ 2) SHE where the lower-rank spin and charge currents are zero. Here the rank of the spin current is defined through the spin tensor matrix rank in the spin current operator. If so, can the higher-rank spin-Hall conductivity be a universal constant independent of material properties? Can we realize and observe higher-rank SHE in a realistic physical system?

In this Letter, we address these important questions by defining and characterizing *universal intrinsic higher-rank SHE*, and exploring the corresponding experimental

realization using cold atoms. Our main results are:

i) We define spin currents of different ranks in a spin-1 system and introduce the concept of rank-2 SHE. Higher-rank SHE for arbitrary spin- F can be defined in a similar manner.

ii) We develop a minimum spin-1 model for realizing rank-2 SHE with intrinsic 2D spin-tensor-momentum coupling (STMC). We find that the rank-2 spin-Hall conductivity is a universal constant $e/8\pi$, which is independent of material properties, and both rank-0 charge-Hall and rank-1 spin-Hall conductivities are zero. This is confirmed by solving both spin dynamics and linear response theory. We also showcase another rank-2 SHE in a spin-3/2 model.

iii) We propose an experimental scheme for realizing the 2D STMC in the minimal spin-1 model of rank-2 SHE. This is done by utilizing ultracold fermions in a 2D optical lattice with STMC, which is built upon recent experimental advances on realizations of 2D SOC for pseudospin-1/2 atoms [3]. We propose that rank-2 SHE can be observed by measuring rank-2 spin accumulations [14].

Rank-2 spin currents and spin-Hall effect. In a spin-1/2 system characterized by the SU(2) group, the spin operators are defined by Pauli matrices σ_i , which are rank-1 spin vectors satisfying $\{\sigma_i, \sigma_j\}_+ = \delta_{ij}$, and do not allow rank-2 spin tensors. In a spin-1 system with the SU(3) group, the rank-1 spin vectors F_i do not satisfy $\{F_i, F_j\}_+ \propto \delta_{ij}$, with rank-2 spin tensors defined as $N_{ij} = \{F_i, F_j\}_+/2 - \delta_{ij}\mathbf{F}^2/3$ [1]. Along the quantization axis z , rank-1 and 2 spin polarization operators can be defined as $P_1 = \hbar F_z$ and $P_2 = \hbar N_{zz}$, leading to spin current density operators $\mathbf{J}_1^z = \frac{1}{2}\{P_1, \mathbf{v}\}_+$ and $\mathbf{J}_2^{zz} = \frac{1}{2}\{P_2, \mathbf{v}\}_+$. The definition naturally yields usual rank-1 spin polarization $\langle F_z \rangle = \psi^\dagger \hbar F_z \psi$ and spin current density $\langle \mathbf{J}_1^z \rangle = \frac{1}{2}\text{Re}[\psi^\dagger \{\hbar F_z, \mathbf{v}\}_+ \psi]$, where ψ is the spinor state of the particle. Note that the charge current $\langle \mathbf{J}_0 \rangle = \text{Re}[\psi^\dagger \mathbf{v} \psi]$ can be treated as the current of rank-0 unit matrix I .

For widely studied intrinsic universal rank-1 SHE for spin-1/2 electrons (illustrated in Fig. 1(a)), the applied electric field induces non-zero transverse currents, which are opposite for spin up and down, due to the intrinsic SOC that serves as opposite effective magnetic fields. Therefore the rank-0 total charge current is zero, but the rank-1 spin current is non-zero. Similarly, we can define rank-2 SHE as that with only non-zero rank-2 spin current (rank-1 spin and rank-0 charge currents both vanish). The corresponding spin current configuration is illustrated in Fig. 1(b), where both spin $|+1\rangle$ and $|-1\rangle$ move in the same direction for vanishing rank-1 spin current, while a doubled spin $|0\rangle$ current flows in the opposite direction for the sake of zero charge current. The resulting rank-2 spin current, defined through $N_{zz} = F_z^2 - \frac{2}{3} = \text{diag}(1/3, -2/3, 1/3)$, is clearly non-zero

due to the current directions of three spin components.

Universal intrinsic rank-2 spin-Hall effect. A general form of SOC in a spin-1 system may lead to non-zero spin currents with different ranks. In order to find suitable SOC for rank-2 SHE, we adopt the Gell-Mann matrix representation λ_i , $1 \leq i \leq 8$ for the SU(3) group, which can be grouped into three different SU(2) subalgebras [37]

$$\boldsymbol{\tau}_T = \{\lambda_1, \lambda_2, \lambda_3\}, \boldsymbol{\tau}_U = \{\lambda_4, \lambda_5, \lambda_+\}, \boldsymbol{\tau}_V = \{\lambda_6, \lambda_7, \lambda_-\}. \quad (1)$$

in the two-spin subspaces $\{|+1\rangle, |0\rangle\}_T$, $\{|+1\rangle, |-1\rangle\}_U$ and $\{|0\rangle, |-1\rangle\}_V$. Here $\lambda_\pm = \frac{\sqrt{3}}{2}\lambda_8 \pm \frac{1}{2}\lambda_3$. Spin-1 vectors are related as $F_x = (\lambda_1 + \lambda_6)/\sqrt{2}$, $F_y = (\lambda_2 + \lambda_7)/\sqrt{2}$, and $F_z = \lambda_+$. Physically, each subalgebra spans the symmetry group of an effective quantum spin-1/2 in the two-spin subspace and works as the Pauli matrices.

For each SU(2) subalgebra, we consider the intrinsic SHE with Rashba SOC [16]

$$H_\alpha^{\text{Rashba}} = \frac{p^2}{2m^*} - \frac{\lambda}{\hbar} \boldsymbol{\tau}_\alpha \cdot (\hat{\mathbf{z}} \times \mathbf{p}), \quad (2)$$

where m^* is the effective mass of electron, $\lambda > 0$ is the Rashba coupling strength, and $\alpha = T, U, V$. When the electric field E_x is applied along the x direction (Fig. 1), there is a rank-1 spin Hall conductivity $\sigma_{xy}^z = \frac{e}{8\pi}$ for $\alpha = T, V$ [16]. Note that $\sigma_{xy}^z = \frac{e}{4\pi}$ for $\alpha = U$ because the subalgebra is in the subspace spanned by $\{|+1\rangle, |-1\rangle\}_U$ with doubled spin difference $2\hbar$.

The rank-2 spin-Hall conductivity can be computed using the Kubo formula

$$\sigma_{xy}^{zz} = -e\hbar \int \frac{d^2\mathbf{k}}{(2\pi)^2} \Omega_{xy}^{zz} \quad (3)$$

where $\Omega_{xy}^{zz} = -\sum_{m \neq m'} (f_{m'\mathbf{k}} - f_{m\mathbf{k}}) \frac{\text{Im}\langle m'\mathbf{k} | J_{2,x}^{zz} | m\mathbf{k} \rangle \langle m\mathbf{k} | \mathbf{v}_y | m'\mathbf{k} \rangle}{(E_{m\mathbf{k}} - E_{m'\mathbf{k}})^2}$ is the generalized rank-2 Berry curvature, m and m' are band indices, $f_{m\mathbf{k}} = [e^{(E_{m\mathbf{k}} - E_F)/k_B T} + 1]^{-1}$ is the Fermi-Dirac distribution, the velocity operator $\mathbf{v} = \partial_{\mathbf{p}} H$, and $J_{2,x}^{zz}$ is the x component of the rank-2 spin-Hall current operator. Here $E_{m\mathbf{k}}$ and $|m\mathbf{k}\rangle$ are eigenvalues and eigenvectors in the momentum space.

The three SU(2) subalgebras are not independent. Through blending two of the subalgebras, we construct the following Hamiltonian

$$H_{F=1} = \frac{p^2}{2m^*} - \frac{1}{\sqrt{2}} \frac{\lambda}{\hbar} (\boldsymbol{\tau}_T + \boldsymbol{\tau}_V^*) \cdot (\hat{\mathbf{z}} \times \mathbf{p}), \quad (4)$$

where $(\boldsymbol{\tau}_T + \boldsymbol{\tau}_V^*) \cdot (\hat{\mathbf{z}} \times \mathbf{p}) = p \begin{pmatrix} 0 & -ie^{-i\theta_{\mathbf{p}}} & 0 \\ ie^{i\theta_{\mathbf{p}}} & 0 & ie^{i\theta_{\mathbf{p}}} \\ 0 & -ie^{-i\theta_{\mathbf{p}}} & 0 \end{pmatrix}$ describes a 2D STMC. The resulting band structure is plotted in Fig. 2(a), which exhibits a 2D triply-degenerate point at $\mathbf{p} = 0$. When the Fermi level lays above the

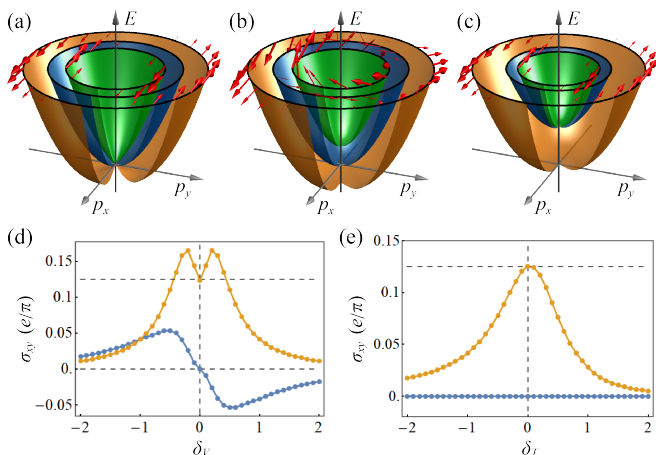


FIG. 2. (a-c) Representative energy bands of the STMC Fermi gas described by Eq. (4) with (a) no Zeeman field, (b) spin vector Zeeman field $\delta_V F_z$, and (c) spin tensor Zeeman field $\delta_T F_z^2$. Red arrows depict the spin textures on the Fermi surfaces. (d) and (e) Rank-1 (blue) and rank-2 (orange) spin-Hall conductivities with respect to vector and tensor Zeeman fields δ_V and δ_T . $E_F = 1$ and $p_F = 1$ are taken as units for energy and momentum. The corresponding dimensionless parameters are set as $m = 0.2$ and $\lambda = 0.5$.

triply-degenerate point, the Fermi surfaces are simply concentric circles due to isotropic SOC, as shown in Fig. 2(a).

Applying the Kubo formula with $\mathbf{J}_2^{zz} = \frac{1}{2}\{\hbar N_{zz}, \mathbf{v}\}$, we find a non-vanishing rank-2 spin-Hall conductivity [38]

$$\sigma_{xy}^{zz} = \frac{e}{8\pi}, \quad (5)$$

when the Fermi level lays above the triply-degenerate point, while charge and rank-1 spin Hall conductivities $\sigma_{xy}^c = \sigma_{xy}^z = 0$. We note that $\sigma_{xy}^{zz} = \frac{e}{8\pi}$ is a universal constant that is independent of the material parameters such as SOC strength and effective mass. Therefore the model Hamiltonian Eq. (4) describes a simple yet non-trivial system exhibiting universal higher-rank SHE.

To understand the physical mechanism of this rank-2 SHE, we notice that $\boldsymbol{\tau}_T \cdot (\hat{\mathbf{z}} \times \mathbf{p})$ yields a rank-1 SHE where $|+1\rangle$ and $|0\rangle$ spin components move in opposite transverse directions (see Fig. 1(b)), rendering a rank-1 spin-Hall conductivity $\sigma_{xy}^T = \frac{e}{8\pi}$. Accordingly, the conjugate term $\boldsymbol{\tau}_T^* \cdot (\hat{\mathbf{z}} \times \mathbf{p})$ leads to an opposite spin flow, yielding a negative $\sigma_{xy}^{T^*} = -\frac{e}{8\pi}$. While this can be verified by the Kubo formula, a more insightful way is to look at the Bloch equation [16]

$$\hbar \frac{d\mathbf{n}}{dt} = \mathbf{n} \times \boldsymbol{\Delta} + \eta_d \hbar \frac{d\mathbf{n}}{dt} \times \mathbf{n}, \quad (6)$$

where \mathbf{n} is the direction of the doublet, $\boldsymbol{\Delta}$ is the Zeeman coupling (i.e. the SOC term) and η_d is some small damping effects. Considering the region where linear response theory applies and keeping only leading-order terms, we

have

$$n_z = -\frac{e\hbar^2 E_x p_y}{2\lambda p^3}, \quad (7)$$

whose sign can be reversed by changing that of p_y . Notice that

$$\boldsymbol{\tau}_T^* \cdot (\hat{\mathbf{z}} \times \mathbf{p}) = \boldsymbol{\tau}_T \cdot (\hat{\mathbf{z}} \times (\mathcal{I}\mathbf{p}\mathcal{I}^{-1})), \quad (8)$$

where \mathcal{I} denotes spatial inversion under which $\mathbf{p} \rightarrow -\mathbf{p}$. Therefore n_z gains an opposite sign between Rashba SOC and its conjugate term, leading to opposite rank-1 spin Hall conductivities. Similar argument also applies to other subalgebras $\boldsymbol{\tau}_U$ and $\boldsymbol{\tau}_V$.

From above argument, $\boldsymbol{\tau}_V^*$ conjugate Rashba spin-orbit coupling dictates that the $|0\rangle/|-1\rangle$ components flow along the same direction as the $|0\rangle/|+1\rangle$ components under $\boldsymbol{\tau}_T$ (Fig. 1(b)). Therefore, Eq. (4) can be understood as coupled Rashba SOC and its conjugate in different spin subspaces spanned, respectively, by $\{|+1\rangle, |0\rangle\}_T$ and $\{|0\rangle, |-1\rangle\}_V$ (Fig. 1(b)). The STMC term with $\boldsymbol{\tau}_T + \boldsymbol{\tau}_V^*$ leads to the rank-2 spin-Hall conductivity $\sigma_{xy}^{zz} = \frac{e}{8\pi}$, while both rank-0 charge-Hall and rank-1 spin-Hall conductivities vanish, as shown in Figs. 2(d) and 2(e). More intuitively, the coupling between $\boldsymbol{\tau}_T$ and $\boldsymbol{\tau}_V^*$ terms mediated by the shared $|0\rangle$ guarantees the coherent spin current of $\frac{1}{\sqrt{2}}(|+1\rangle + |-1\rangle)$ flowing in the opposite direction to that of $|0\rangle$. The coherent spin current and the rank-2 spin-Hall conductivity can also be derived under a gauge transform that rotates the spin quantization axis from z to x direction (see Supplementary materials [38]).

Besides the rank-2 spin current \mathbf{J}_2^{zz} , we can similarly define other higher-rank currents like \mathbf{J}_2^{xy} or \mathbf{J}_2^{yz} , and the corresponding Hall conductivities usually vanish in the above model. However, we notice the following constraint

$$\sigma_{xy}^{xx} + \sigma_{xy}^{yy} + \sigma_{xy}^{zz} = 0 \quad (9)$$

holds as long as the charge current is zero. This constraint can be easily proved since \mathbf{F}^2 must be a multiple of unit matrix (i.e., the total spin is conserved). Applying the Kubo formula, we find

$$\sigma_{xy}^{xx} = 0 \text{ and } \sigma_{xy}^{yy} = -\frac{e}{8\pi}, \quad (10)$$

which indeed satisfies the above constraint.

When $\boldsymbol{\tau}_T + \boldsymbol{\tau}_V^*$ in Eq. (4) changes to $\boldsymbol{\tau}_T + \boldsymbol{\tau}_V$, the STMC transforms into the SOC, i.e., $-\frac{\lambda}{\hbar} \mathbf{F} \cdot (\hat{\mathbf{z}} \times \mathbf{p})$ [6], and there is only rank-1 SHE based on above argument, where the current of spin component $|0\rangle$ is cancelled out. Apply the Kubo formula, we find $\sigma_{xy}^z = \frac{e}{2\pi}$, which counts the spin currents from the counterflow of both $|+1\rangle/|0\rangle$ and $|+1\rangle/|-1\rangle$. Moreover, all rank-2 spin Hall conductivities vanish so that Eq. (9) is trivially satisfied.

Effect of Zeeman fields. Generally, for a spin-1 system discussed above, the Zeeman fields contain both spin-vector and spin-tensor terms as $\delta_V \hbar F_z + \delta_T \hbar F_z^2$. Both

fields lift the triply-degenerate point at $\mathbf{p} = 0$ and spoil the universality of the spin Hall conductivity, as shown in Fig. 2(b)-2(e). We numerically compute the rank-1 and rank-2 spin-Hall conductivities, which are displayed as a function of δ_V and δ_T in Figs. 2(d) and 2(e), respectively, for a given Fermi energy.

Changing the sign of δ_V is equivalent to a \mathbb{Z}_2 rotation between spin components $|+1\rangle$ and $|-1\rangle$, under which spin-tensor polarization $\hbar\langle N_{zz} \rangle$ is unchanged while spin-vector polarization $\hbar\langle F_z \rangle$ gains a minus sign, indicating symmetric and antisymmetric responses from σ_{xy}^{zz} and σ_{xy}^z , as shown in Fig. 2(d). When $|\delta_V|$ increases, both $|\sigma_{xy}^z|$ and $|\sigma_{xy}^{zz}|$ increase to their maxima and then decrease. σ_{xy}^{zz} drops more rapidly as the top band shifts away from the Fermi level. When $\delta_V \rightarrow \pm\infty$, both conductivities approach 0 since the system becomes a flat-band insulator.

The tensor Zeeman field $\delta_T F_z^2$ has the same effect on $|+1\rangle$ and $|-1\rangle$, therefore σ_{xy}^{zz} is asymmetric while σ_{xy}^z remains zero [see Fig. 2(e)]. There would also be small non-zero charge-current conductance, which is not plotted in the panel. When $\delta_T > 0$, it shifts both top and bottom bands upward and they remain degenerate at $\mathbf{p} = 0$, as shown in Fig. 2(c). When $\delta_T > E_F$, the upper two bands are lifted above the Fermi energy, while the three bands remain intersecting the Fermi level for $\delta_T < 0$. Therefore, the rank-2 spin-Hall conductivity σ_{xy}^{zz} decays faster in the positive branch than that in the negative branch, as shown in Fig. 2(e).

Generalization to larger spin. A rank-2 SHE can also be realized in a spin-3/2 system. Consider a 2D spin-3/2 Hamiltonian

$$H_{F=\frac{3}{2}} = \frac{p^2}{2m^*} - \frac{\lambda}{\hbar}(\boldsymbol{\tau}_{1,2} + \boldsymbol{\tau}_{3,4}^*) \cdot (\hat{\mathbf{z}} \times \mathbf{p}), \quad (11)$$

where $\boldsymbol{\tau}_{1,2}$ and $\boldsymbol{\tau}_{3,4}$ represent SU(2) subalgebra for $|m_z > 0\rangle$ and $|m_z < 0\rangle$ respectively [38]. The Hamiltonian is block-diagonalized since the spin components $|m_z > 0\rangle$ or $|m_z < 0\rangle$ are coupled separately. The Hamiltonian describes two decoupled rank-1 SHEs defined by $\tau_{1,2,z}$ and $\tau_{3,4,z}$ in two subspaces. Specifically, spin components $|m_z\rangle$ and $|-m_z\rangle$ flow along the same direction, which is opposite to that of $|m_z \pm 2\rangle$ (- for $m_z > 0$ and + for $m_z < 0$). Consequently, there is only non-vanishing rank-2 spin current with Hall conductivity $\sigma_{xy}^{zz} = \frac{e}{2\pi}$.

Higher-rank SHE for arbitrary spin- F can be defined similarly using the algebra of SU($N = 2F + 1$) group (see supplementary material [38]). The maximum rank of SHE is $N - 1$, and spin current is defined using the higher-rank spin tensor similar as N_{zz} . For a general SU(N) group, we can use the generalized Gell-Mann matrices [2], from which the SU(2) subalgebras could be defined. Hamiltonians for realizing different ranks of SHEs may be constructed similarly using the SOC based on such SU(2) subgroups.

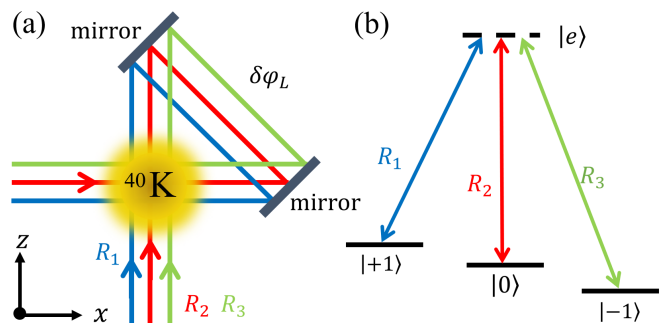


FIG. 3. Illustration of the experimental scheme for realizing STMC for the rank-2 SHE in Eq. (4). (a) Laser setup consisting of three Raman lasers R_1 (Blue, plane-wave), R_2 (red, standing wave) and R_3 (green, plane wave). φ_L denotes the phase accumulated by lasers in the triangle optical path K formed by the atomic gas and two mirrors. Then $\delta\varphi_L$ is the differences between the accumulated phase. (b) The coupling between three spin states under the Raman lasers with proper frequencies.

Potential experimental realization and detection. Recently, 2D SOC for spin-1/2 systems has been experimentally realized in cold atoms [3, 4, 41]. Here we propose that similar experimental setup [3] can also be used to realize the STMC in the model Hamiltonian Eq. (4) using a pseudospin-1 ultracold atomic gas.

We use three hyperfine states of atoms to define (pseudo)spin states $|+1\rangle$, $|0\rangle$, and $|-1\rangle$. As demonstrated in Ref. [3], either $\boldsymbol{\tau}_T \cdot (\hat{\mathbf{z}} \times \mathbf{p})$ or $\boldsymbol{\tau}_V^* \cdot (\hat{\mathbf{z}} \times \mathbf{p})$ can be realized in subspaces $\{|+1\rangle, |0\rangle\}_T$ or $\{|0\rangle, |-1\rangle\}_V$ by applying the Raman coupling between two spin states using a standing-wave and a plane-wave Raman lasers. For the experiment from Ref. [3], different forms of the SOC are tuned by adjusting a phase term $\delta\varphi_L$, which is the accumulated relative phase between two Raman beams when both travel through a given optical path. $\boldsymbol{\tau}_T$ and $\boldsymbol{\tau}_V^*$ terms correspond to $\delta\varphi_L = \frac{\pi}{2}$ and $-\frac{\pi}{2}$, respectively.

In order to generate coherent superposition of two different spin-orbit couplings in different subspaces, two plane-wave and one standing-wave Raman lasers are used to couple $\{|+1\rangle, |0\rangle\}_T$ and $\{|0\rangle, |-1\rangle\}_V$, respectively, as illustrated in Fig. 3. Because of different forms of SOC $\boldsymbol{\tau}_T$ and $\boldsymbol{\tau}_V^*$ in different subspaces, we need $\delta\varphi_L = -\frac{\pi}{2}$ for $\{|+1\rangle, |0\rangle\}_T$ and $\frac{\pi}{2}$ for $\{|0\rangle, |-1\rangle\}_V$ using the same optical path. However, the phase tuning is unrealistic here due to the small frequency difference between R_1 and R_3 . We circumvent this issue by choosing the laser frequency configuration in Fig. 3(b). Here the blue plane-wave R_1 and red standing wave R_2 induce the Raman coupling $\sim \Omega_{R_1}\Omega_{R_2}^*$ between $|+1\rangle$ and $|0\rangle$, while the red standing wave R_2 and green plane-wave R_3 induce the coupling $\sim \Omega_{R_2}\Omega_{R_3}^*$ between $|0\rangle$ and $|-1\rangle$. Ω_{R_i} is the Rabi frequency for corresponding Raman laser R_i . When $\Omega_{R_1} = \Omega_{R_3}$, the complex conjugate condition could be satisfied, which realizes the desired STMC in Hamilto-

nian Eq. (4).

To trigger the rank-2 SHE, an effective electric field for driving cold atoms into motion can be achieved by applying a bias potential. The rank-2 spin current generated by the counterflow of $|0\rangle$ and $\frac{1}{\sqrt{2}}|+1\rangle + \frac{1}{\sqrt{2}}|-1\rangle$ leads to the accumulation of the two states at opposite lateral edges, as illustrated in Fig. 1(b). The spin accumulation can be detected as the signature of the rank-2 SHE, similar as that for rank-1 SHE [14]. More details about the experimental scheme can be found in the supplementary materials [38].

Discussions and Conclusions. There are other types of SOC, besides the discussed Rashba-type $\boldsymbol{\tau} \cdot (\hat{\mathbf{z}} \times \mathbf{p})$, leading to higher-rank SHE as well. For instance, we can mix Dresselhaus and Rashba types in a spin-1 Hamiltonian

$$H_{\text{Mix}} = \frac{\mathbf{p}^2}{2m^*} - \frac{1}{\sqrt{2}} \frac{\lambda}{\hbar} ((\boldsymbol{\tau}_T \cdot (\hat{\mathbf{z}} \times \mathbf{p}) + \boldsymbol{\tau}_V \cdot \mathbf{p}), \quad (12)$$

which yields a universal intrinsic rank-2 SHE with $\sigma_{xy}^{zz} = \frac{e}{8\pi}$. In general, the characterization and symmetry requirement of the SOC for realizing higher-rank SHEs would be an interesting topic to study.

In conclusion, we introduce and characterize the concept of higher-rank SHE in large spin systems and propose its experimental realization in cold atomic systems. There are many physics remaining to be explored, such as the general construction of rank- n SHE in arbitrary spin systems, quantized higher-rank SHE that will enrich the category of topological insulators [42], the effects of many-body interaction or disorders, extrinsic higher-rank SHE, experimental proposal in solid-state materials with exotic effective pseudospin-1 fermions in 2D [43], and the observation of higher-rank SHE in the parameter space [24, 35], etc. Our work defines a new class of SHEs and opens the door for designing large-spin devices with novel functionalities for spintronic applications.

Acknowledgements: We thank Fan Zhang for helpful discussion. This work was supported by Air Force Office of Scientific Research (FA9550-16-1-0387, FA9550-20-1-0220), National Science Foundation (PHY-1806227), and Army Research Office (W911NF-17-1-0128).

* These authors contributed equally to this work

† Email: chuanwei.zhang@utdallas.edu

- [1] J. E. Hirsch, Spin Hall Effect, *Phys. Rev. Lett.* **83**, 1834 (1999).
- [2] J. Sinova, S. O. Valenzuela, J. Wunderlich, C. H. Back, and T. Jungwirth, Spin Hall effects, *Rev. Mod. Phys.* **87**, 1213 (2015).
- [3] T. Seki et al., Giant spin Hall effect in perpendicularly spin-polarized FePt/Au devices, *Nat. Mater.* **7**, 125 (2008).
- [4] L. Liu et al., Spin-Torque Switching with the Giant Spin Hall Effect of Tantalum, *Science* **336**, 555 (2012).
- [5] Y. Niimi et al., Giant Spin Hall Effect Induced by Skew Scattering from Bismuth Impurities inside Thin Film CuBi Alloys, *Phys. Rev. Lett.* **109**, 156602 (2012).
- [6] E. Saitoh, M. Ueda, and H. Miyajima, Conversion of spin current into charge current at room temperature: Inverse spin-Hall effect, *Appl. Phys. Lett.* **88**, 182509 (2006).
- [7] T. Kimura, Y. Otani, T. Sato, S. Takahashi, and S. Maekawa, Room-Temperature Reversible Spin Hall Effect, *Phys. Rev. Lett.* **98**, 156601 (2007).
- [8] B. F. Miao, S. Y. Huang, D. Qu, and C. L. Chien, Inverse Spin Hall Effect in a Ferromagnetic Metal, *Phys. Rev. Lett.* **111**, 066602 (2013).
- [9] J.-C. Rojas-Sánchez et al., Spin Pumping and Inverse Spin Hall Effect in Platinum: The Essential Role of Spin-Memory Loss at Metallic Interfaces, *Phys. Rev. Lett.* **112**, 106602 (2014).
- [10] M. Kimata et al., Magnetic and magnetic inverse spin Hall effects in a non-collinear antiferromagnet, *Nature* **565**, 627(2019).
- [11] C. L. Kane and E. J. Mele, Quantum Spin Hall Effect in Graphene, *Phys. Rev. Lett.* **95**, 226801 (2005).
- [12] B. A. Bernevig, T. L. Hughes, S.-C. Zhang, Quantum Spin Hall Effect and Topological Phase Transition in HgTe Quantum Wells, *Science* **314**, 1757 (2006).
- [13] M. König, S. Wiedmann, C. Brune, A. Roth, H. Buhmann, L. W. Molenkamp, X.-L. Qi, S.-C. Zhang, Quantum Spin Hall Insulator State in HgTe Quantum Wells, *Science* **318**, 766 (2007).
- [14] Y. K. Kato, R. C. Myers, A. C. Gossard, D. D. Awschalom, Observation of the Spin Hall Effect in Semiconductors, *Science* **306**, 1910 (2004).
- [15] S. Murakami, N. Nagaosa, and S. C. Zhang, Dissipationless Quantum Spin Current at Room Temperature, *Science* **301**, 1348 (2003).
- [16] J. Sinova, D. Culcer, Q. Niu, N. A. Sinitsyn, Universal Intrinsic Spin Hall Effect, *Phys. Rev. Lett.* **92**, 126603 (2004).
- [17] Y. Kawaguchi and M. Ueda, Spinor Bose-Einstein condensates, *Phys. Rep.* **520**, 253 (2012).
- [18] B. Bradlyn et al., Beyond Dirac and Weyl fermions: Unconventional quasiparticles in conventional crystals, *Science* **353**, 6299 (2016).
- [19] H. Hu, J. Hou, F. Zhang, and C. Zhang, Topological Triply Degenerate Points Induced by Spin-Tensor-Momentum Couplings, *Phys. Rev. Lett.* **120**, 240401 (2018).
- [20] B. Q. Lv et al., Observation of three-component fermions in the topological semimetal molybdenum phosphide, *Nature* **546**, 627 (2017).
- [21] D. L. Campbell, R. M. Price, A. Putra, A. Valdés-Curiel, D. Trypogeorgos & I. B. Spielman, Magnetic phases of spin-1 spin-orbit-coupled Bose gases, *Nat. Commun.* **7**, 10897 (2016).
- [22] X. Luo, L. Wu, J. Chen, Q. Guan, K. Gao, Z.-F. Xu, L. You & R. Wang, Tunable atomic spin-orbit coupling synthesized with a modulating gradient magnetic field, *Sci. Rep.* **6**, 18983 (2016).
- [23] T. Ollikainen, A. Blinova, M. Möttönen, and D. S. Hall, Decay of a Quantum Knot, *Phys. Rev. Lett.* **123**, 163003 (2019).
- [24] X. Tan, D.-W. Zhang, Q. Liu, G. Xue, H.-F. Yu, Y.-Q. Zhu, H. Yan, S.-L. Zhu, and Y. Yu, Topological Maxwell Metal Bands in a Superconducting Qutrit, *Phys. Rev. Lett.* **120**, 130503 (2018).

- [25] K. Sun, C. Qu, Y. Xu, Y. Zhang, and C. Zhang, Interacting spin-orbit-coupled spin-1 Bose-Einstein condensates, *Phys. Rev. A* **93**, 023615 (2016).
- [26] Z.-Q. Yu, Phase transitions and elementary excitations in spin-1 Bose gases with Raman-induced spin-orbit coupling, *Phys. Rev. A* **93**, 033648 (2016).
- [27] G. I. Martone, F. V. Pepe, P. Facchi, S. Pascazio, and S. Stringari, Tricriticalities and Quantum Phases in Spin-Orbit-Coupled Spin-1 Bose Gases, *Phys. Rev. Lett.* **117**, 125301 (2016).
- [28] X.-W. Luo, K. Sun, and C. Zhang, Spin-Tensor-Momentum-Coupled Bose-Einstein Condensates, *Phys. Rev. Lett.* **119**, 193001 (2017).
- [29] E. J. König and J. H. Pixley, Quantum Field Theory of Nematic Transitions in Spin-Orbit-Coupled Spin-1 Polar Bosons, *Phys. Rev. Lett.* **121**, 083402 (2018).
- [30] M. Naghiloo, M. Abbasi, Y. N. Joglekar, K. W. Murch, Quantum state tomography across the exceptional point in a single dissipative qubit, *Nat. Phys.* **15**, 1232 (2018)
- [31] I. Kuzmenko, T. Kuzmenko, Y. Avishai, and M. Sato, Spin-orbit coupling and topological states in an $F = \frac{2}{3}$ cold Fermi gas, *Phys. Rev. B* **98**, 165139 (2018).
- [32] J. Hou, H. Hu, C. Zhang, Topological phases in pseudospin-1 Fermi gases with two-dimensional spin-orbit coupling, *Phys. Rev. B* **101**, 053613 (2020).
- [33] G. Palumbo and N. Goldman, Revealing Tensor Monopoles through Quantum-Metric Measurements, *Phys. Rev. Lett.* **121**, 170401 (2018).
- [34] G. Palumbo and N. Goldman, Tensor Berry connections and their topological invariants, *Phys. Rev. B* **99**, 045154 (2019).
- [35] X. Tan, D.-W. Zhang, W. Zheng, X. Yang, S. Song, Z. Han, Y. Dong, Z. Wang, D. Lan, H. Yan, S.-L. Zhu, and Y. Yu, Experimental Observation of Tensor Monopoles with a Superconducting Qudit, *Phys. Rev. Lett.* **126**, 017702 (2021).
- [36] Z. Wu et al., Realization of two-dimensional spin-orbit coupling for Bose-Einstein condensates, *Science* **354**, 83 (2016).
- [37] Robert N. Cahn, *Semi-Simple Lie Algebras and Their Representations*, Benjamin/Cummings (1984).
- [38] See supplementary materials for details about SU(2) subalgebras of SU(N), experimental proposals and how to detect rank-2 SHEs in experiments.
- [39] G. Kimura, The Bloch vector for N-level systems, *Phys. Lett. A* **314**, 339 (2003).
- [40] L. H. Huang et al., Experimental realization of two-dimensional synthetic spin-orbit coupling in ultracold Fermi gases, *Nat. Phys.* **12**, 540 (2016).
- [41] Z. Meng et al., Experimental observation of a topological band gap opening in ultracold Fermi gases with two-dimensional spin-orbit coupling, *Phys. Rev. Lett.* **117**, 235304 (2016).
- [42] M. Z. Hasan and C. L. Kane, Colloquium: Topological insulators, *Rev. Mod. Phys.* **82**, 3045 (2010).
- [43] S.-S. Wang et al., Monolayer Mg₂C: Negative Poisson's ratio and unconventional two-dimensional emergent fermions, *Phys. Rev. Materials* **2**, 104003 (2018).

Supplemental Material for "Intrinsic high-rank spin Hall effect"

S1: Derivation of the rank-2 spin-Hall conductivity. Diagonalizing the Hamiltonian Eq. (4) of the main text yields three eigenstates

$$|1\mathbf{k}\rangle = \begin{pmatrix} \frac{1}{2} \\ \frac{i}{\sqrt{2}}e^{i\theta_{\mathbf{k}}} \\ \frac{1}{2} \end{pmatrix}, \quad |2\mathbf{k}\rangle = \begin{pmatrix} \frac{1}{\sqrt{2}} \\ 0 \\ -\frac{1}{\sqrt{2}} \end{pmatrix}, \quad |3\mathbf{k}\rangle = \begin{pmatrix} -\frac{1}{2} \\ \frac{i}{\sqrt{2}}e^{i\theta_{\mathbf{k}}} \\ \frac{1}{2} \end{pmatrix}, \quad (\text{S1})$$

where $\theta_{\mathbf{k}}$ is the polar angle of the wavevector \mathbf{k} , with the corresponding eigenenergies

$$E_{1\mathbf{k}} = \frac{\hbar^2 k^2}{2m} - \lambda k, \quad E_{2\mathbf{k}} = \frac{\hbar^2 k^2}{2m}, \quad E_{3\mathbf{k}} = \frac{\hbar^2 k^2}{2m} + \lambda k. \quad (\text{S2})$$

Then we substitute the eigenstates and eigenenergies into the Kubo formula Eq. (3) to calculate the rank-2 spin-Hall conductivity σ_{xy}^{zz} . Here we consider zero temperature such that the Fermi-Dirac distribution is a step function. The momentum space is divided into four different regions I-IV that are separated by the three concentric Fermi surfaces, as shown in Fig. S1. In region I (IV), all energy bands are occupied (empty) with the Fermi-Dirac function $f_{1,2,3\mathbf{k}} = 1$ ($f_{1,2,3\mathbf{k}} = 0$). Therefore regions I and IV have no contribution to the rank-2 spin-Hall conductivity according to the Kubo formula Eq. (3). In region II, energy bands $E_{1,2\mathbf{k}}$ are occupied while band $E_{3\mathbf{k}}$ is empty. In region III, energy band $E_{1\mathbf{k}}$ is occupied while bands $E_{2,3\mathbf{k}}$ are empty. Thus the Kubo formula becomes

$$\begin{aligned} \sigma_{xy}^{zz} &= \frac{e\hbar}{4\pi^2} \sum_{m=1,2} \int_{\text{II}} d^2\mathbf{k} \frac{2\text{Im}\langle m\mathbf{k}|J_{2,x}^{zz}|3\mathbf{k}\rangle\langle 3\mathbf{k}|v_y|m\mathbf{k}\rangle}{(E_{3\mathbf{k}} - E_{m\mathbf{k}})^2} + \frac{e\hbar}{4\pi^2} \sum_{m=2,3} \int_{\text{III}} d^2\mathbf{k} \frac{2\text{Im}\langle 1\mathbf{k}|J_{2,x}^{zz}|m\mathbf{k}\rangle\langle m\mathbf{k}|v_y|1\mathbf{k}\rangle}{(E_{m\mathbf{k}} - E_{1\mathbf{k}})^2} \\ &= \frac{e\hbar}{4\pi^2} \int_{\text{II+III}} d^2\mathbf{k} \frac{\hbar}{4M\lambda} \frac{k_x^2}{k^3} = \frac{e\hbar^2}{16\pi^2 M\lambda} \int_{k_{F3}}^{k_{F1}} dk \int d\theta \cos^2 \theta \\ &= \frac{e\hbar^2}{16\pi M\lambda} (k_{F1} - k_{F3}) = \frac{e}{8\pi}, \end{aligned} \quad (\text{S3})$$

where $k_{F1,3}$ are the Fermi wavevectors, as shown in Fig. S1, and $k_{F1} - k_{F3} = 2M\lambda/\hbar^2$. In the first line of Eq. (S3), the factor 2 in front of the integrand comes from the exchange of band indices in the Kubo formula. In the second line, the integration is transformed into the polar coordinate. Our analytical derivation shows that, as long as the Fermi energy is above the triply degenerate point, the rank-2 spin-Hall conductivity is quantized.

S2: Spin dynamics analysis. Because the spin-tensor-momentum coupling (STMC) in Eq. (4) involves both spin tensor and vector, we cannot treat it as an effective Zeeman interaction as that in the Rashba spin orbit coupling. Consequently, the spin magnitude is not conserved, as shown in Fig. 2(a), and the spin dynamics analysis cannot be directly applied. In this section, we develop an effective theory for the spin dynamics by performing a gauge transformation that rotates the spin quantization axis from z to x direction by the unitary transformation

$$UF_xU^{-1} = F_z, \quad UF_yU^{-1} = -F_y, \quad UF_zU^{-1} = F_x, \quad (\text{S4})$$

where the unitary matrix

$$U = \begin{pmatrix} \frac{1}{2} & \frac{1}{\sqrt{2}} & \frac{1}{2} \\ \frac{1}{\sqrt{2}} & 0 & -\frac{1}{\sqrt{2}} \\ \frac{1}{2} & -\frac{1}{\sqrt{2}} & \frac{1}{2} \end{pmatrix}. \quad (\text{S5})$$

Thus the Hamiltonian Eq. (4) of the main text becomes

$$\tilde{H}_{F=1} = UH_{F=1}U^{-1} = \frac{\mathbf{p}^2}{2m} + \frac{\lambda}{\hbar}(p_y\lambda_+ + p_x\lambda_5), \quad (\text{S6})$$

in which the spin state $|\tilde{0}\rangle$ is decoupled with $|\pm\tilde{1}\rangle$ and has the dispersion $\mathbf{p}^2/2m$. Here $|\tilde{-1}\rangle = \frac{1}{2}(|+1\rangle + |-1\rangle) - \frac{1}{\sqrt{2}}|0\rangle$, $|\tilde{0}\rangle = \frac{1}{2}(|+1\rangle - |-1\rangle)$, $|\tilde{1}\rangle = \frac{1}{2}(|+1\rangle + |-1\rangle) + \frac{1}{\sqrt{2}}|0\rangle$ are the spin states quantized along the x direction.

The rank-2 spin tensor becomes

$$\tilde{N}_{zz} = UN_{zz}U^{-1} = \begin{pmatrix} \frac{1}{2} & 0 & \frac{1}{2} \\ 0 & 1 & 0 \\ \frac{1}{2} & 0 & \frac{1}{2} \end{pmatrix} - \frac{2}{3}I \quad (\text{S7})$$

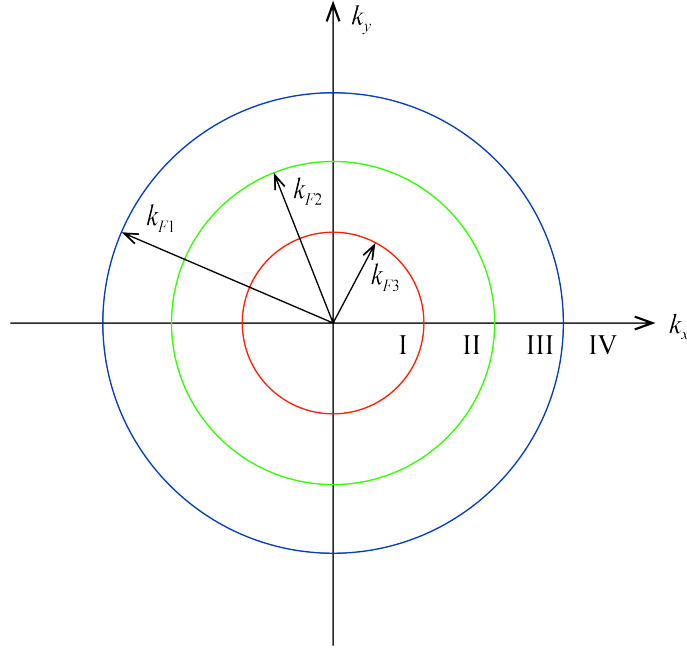


FIG. S1. Schematic of concentric Fermi surfaces. The momentum space is divided into four different regions I-IV by the Fermi surfaces.

under the transformation. Because $\langle \tilde{0} | \mathbf{v} | \pm \tilde{1} \rangle = 0$ where the velocity operator $\mathbf{v} = \partial_{\mathbf{p}} \tilde{H}$, the spin state $|\tilde{0}\rangle$ has no contribution to the rank-2 spin-Hall conductivity, which can be directly inferred from the Kubo formula Eq. (3) of the main text. Therefore, we can focus only on the subspace spanned by $\{|-\tilde{1}\rangle, |+\tilde{1}\rangle\}$. Now we project the Hamiltonian and rank-2 spin tensor onto the subspace

$$P \tilde{H}_{F=1} P = \frac{\mathbf{p}^2}{2m} + \frac{\lambda}{\hbar} (p_y \sigma_z + p_x \sigma_y), \quad (\text{S8})$$

$$P \tilde{N}_{zz} P = \frac{1}{2} \sigma_x - \frac{1}{6} \sigma_0, \quad (\text{S9})$$

where $P = |+\tilde{1}\rangle \langle +\tilde{1}| + |-\tilde{1}\rangle \langle -\tilde{1}|$ is the projection operator. According to Eq. (S8), the spin dynamics are governed by the Bloch equation Eq. (6) of the main text with the \mathbf{p} -dependent Zeeman field $\mathbf{\Delta} = \frac{2\lambda}{\hbar} (0, -p_x, -p_y)$. Under an electric field along the x direction, the y component of the Zeeman field changes as $-\dot{p}_x = eE_x$. Solving the Bloch equation yields the x component of the spin direction that depends on \mathbf{p} as

$$\tilde{n}_x = \frac{e\hbar^2 E_x p_y}{2\lambda p^3}. \quad (\text{S10})$$

Because \tilde{n}_x is an odd function of p_y , there is a transverse rank-2 spin current $J_{2,y}^{zz} = \frac{1}{2} \{ \hbar P \tilde{N}_{zz} P, v_y \}_+$. The electric field tilts the spin texture on the Fermi surface according to Eq. (S10), as shown in Fig. S2. Note that the spin texture here is different from that in Fig. 2(a) because it is obtained by the gauge transformation and projecting out the $|\tilde{0}\rangle$ state. The rank-2 SHE leads to the counterflow of currents of $\frac{1}{\sqrt{2}} |+\tilde{1}\rangle \pm \frac{1}{\sqrt{2}} |-\tilde{1}\rangle$ which transform back into

$$\begin{aligned} U^{-1} \left(\frac{1}{\sqrt{2}} |+\tilde{1}\rangle + \frac{1}{\sqrt{2}} |-\tilde{1}\rangle \right) &= \frac{1}{\sqrt{2}} |+1\rangle + \frac{1}{\sqrt{2}} |-1\rangle, \\ U^{-1} \left(\frac{1}{\sqrt{2}} |+\tilde{1}\rangle - \frac{1}{\sqrt{2}} |-\tilde{1}\rangle \right) &= |0\rangle, \end{aligned} \quad (\text{S11})$$

whose spin quantization axis is along the z direction. Because both two states have zero expectation value of F_z , the rank-1 spin-Hall conductivity vanishes.

S3: Higher-rank SHE for arbitrary spin- F . Mathematically, it is well-known that a spin- F Hamiltonian can be expanded using the generators of the $SU(N = 2F + 1)$ group. Those generators are traceless and symmetric, and can

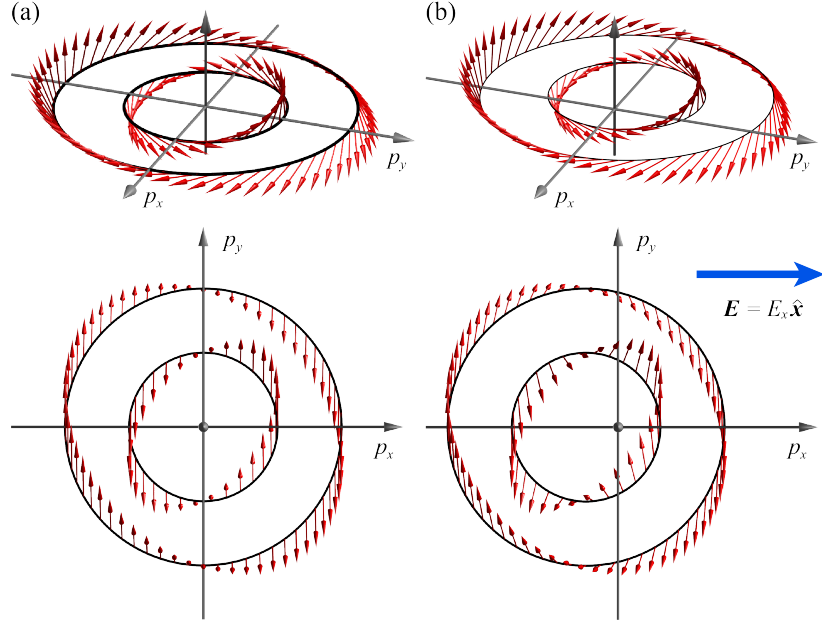


FIG. S2. (a) and (b) Spin texture on the Fermi surfaces with and without an electric field in the x direction. The upper panels show the bird view of the spin texture, while the lower panels are the top view. The electric field shifts the Fermi surfaces to the negative p_x direction by $\sim eE_x\tau/\hbar$ where τ is the mean free time. The electric field tilts the spins with positive (negative) p_y on the Fermi surfaces to the positive (negative) x direction.

be constructed as rank- n ($n \leq r_s$) spin tensors from spin vectors F_i , $i = x, y, z$. Here $r_s = N - 1$ is the rank of $SU(N)$ group. For instance, there are up to rank-2 spin tensors defined as $N_{ij} = \{F_i, F_j\}_+ / 2 - \delta_{ij} \mathbf{F}^2 / 3$ in a spin-1 system [S1]. We use a Cartan subalgebra $\{F_z, N_{zz}, \dots, N_{zz\dots z}\}$ of $SU(N)$ to define a rank- n spin polarization $P_n = \hbar N_{zz\dots z}$ (with n subscripts) and spin current density $\mathbf{J}_n^{zz\dots z} = \frac{1}{2} \{P_n, \mathbf{v}\}_+$ operators. We can define rank- n SHE as that with only non-zero rank- n spin current (spin currents with different ranks, including charge current, all vanish). Clearly, the first example is the rank-2 SHE, which requires at least a spin-1 system.

For a general $SU(N)$ group, we can use the generalized Gell-Mann matrices [S2], from which the $SU(2)$ subalgebras could be defined. Consider a $SU(N)$ Lie group, whose defining representation can be expressed as the generalized Gell-Mann Matrix

$$\begin{aligned} \lambda_{j,k}^S &= I_{j,k} + I_{k,j}, \lambda_{j,k}^A = -i(I_{j,k} - I_{k,j}), \\ \lambda_l^D &= \sqrt{\frac{2}{l(l+1)}} \left(\sum_{m=1}^l I_{m,m} - lI_{l+1,l+1} \right), \end{aligned} \quad (\text{S12})$$

where $1 \leq j < k \leq N$, $1 \leq l \leq N - 1$ and $I_{j,k}$ denotes the matrix with a 1 in the (j, k) -th entry and 0 elsewhere. We could similarly write down all different $SU(2)$ subalgebras as

$$\boldsymbol{\tau}_{j,k} = \{\lambda_{j,k}^S, \lambda_{j,k}^A, \mathbf{c}_{j,k}^l, \lambda_l^D\},$$

where $\mathbf{c}_{j,k}$ is some real vector so that the structure constant of the $SU(2)$ subalgebra is maintained.

Similar as the main text for the rank-2 SHE, Hamiltonians for realizing different ranks of SHEs can be constructed using the SOC based on such $SU(2)$ subgroups. Since the Cartan subalgebra is complete up to a constant, this configuration implies that there must be a non-vanishing rank-2 spin current. Such a completeness also guarantees that a rank- n SHE can always be defined.

S4: Experimental realization of STMC. In this section, we discuss the experimental scheme for realizing required spin-tensor-momentum coupling for rank-2 SHE in a pseudospin-1 fermionic cold gas. Both laser configuration and level diagram are illustrated in Fig. S3 with more details. As 2D spin-orbit coupling has been realized in both bosonic and fermionic cold-atom platforms [S3–S5], the proposed experimental scheme can be readily implemented with the state-of-art experimental technologies.

In Fig. S3(a), two beams (red) are incident from both x and z directions and reflected by two mirrors to form standing waves $\mathbf{E}_{2x} = \hat{z}E_{2x}e^{i(\varphi_{2x} + \varphi_{2z} + \varphi_L)/2} \cos(k_0x + \alpha)$ and $\mathbf{E}_{2z} = \hat{x}E_{2z}e^{i(\varphi_{2x} + \varphi_{2z} + \varphi_L)/2} \cos(k_0z + \beta)$, where $E_{2x(z)}$

is field strength, $\varphi_{2x(z)}$ is the initial phase, $\varphi_L = k_0 K$ is the phase picked up from optical path K and $\alpha(\beta) = (\varphi_{2x(z)} - \varphi_{2z(x)} - \varphi_L)/2$. Another two laser beams (blue and green) are incident in z direction as plane waves $\mathbf{E}_{1(3)z} = \hat{x}E_{1(3)z}e^{i(k_0z+\varphi_{1(3)})}$ and $\mathbf{E}_{1(3)x} = \hat{z}E_{1(3)x}e^{i(-k_0x+\varphi_{1(3)}+\varphi_L-\delta\varphi_{L1(3)})}$ with the initial phases $\varphi_{1(3)}$ and relative phases $\delta\varphi_{L1(3)} = (\omega_2 - \omega_{1(3)})K/c$.

A similar scheme has been studied in our previous work [S6], where a low-energy Hamiltonian $k_z F_x + k_x F_y$ has been realized. Such a model describes a rank-1 SHE as we have discussed in the main text. The standing-wave laser will induce a spin-independent lattice potential in this case

$$V(\mathbf{r}) = V_{0x} \cos^2(k_0x + \alpha) + V_{0z} \cos^2(k_0z + \beta), \quad (\text{S13})$$

where $V_{0x(z)}$ are constants. The Raman coupling between $|+1\rangle$ and $|0\rangle$ can be written as

$$M_{1z,2x} = \sum_F \frac{\Omega_{1z,F,9/2}^* \Omega_{2x,F,7/2}}{\Delta_p}, M_{1x,2z} = \sum_F \frac{\Omega_{1x,F,9/2}^* \Omega_{2z,F,7/2}}{\Delta_p},$$

where the effective Rabi frequency is

$$\begin{aligned} \Omega_{ix,F,m_\sigma} &= e \langle \frac{9}{2}, m_\sigma | z | F, m_\sigma \rangle \hat{z} \cdot \mathbf{E}_{ix}, i = 1, 2 \\ \Omega_{1z,F,m_\sigma} &= e \langle \frac{9}{2}, m_\sigma | x | F, m_\sigma + 1 \rangle \hat{x} \cdot \mathbf{E}_{1z}, \Omega_{2z,F,m_\sigma} = \langle \frac{9}{2}, m_\sigma | x | F, m_\sigma - 1 \rangle \hat{x} \cdot \mathbf{E}_{2z} \end{aligned} \quad (\text{S14})$$

and we have neglected the transitions to $D1$ line due to larger fine-structure splitting $\Delta_s \approx 2\pi \times 1.7\text{THz} \gg \Delta_p$. After expanding the effective Rabi frequency, we obtain

$$M_{1z,2x} = M_{0x} \cos(k_0x + \alpha) e^{-i(k_0z+\beta)} e^{i(\varphi_{2z}-\varphi_1)}, \quad (\text{S15})$$

$$M_{1x,2z} = M_{0y} \cos(k_0z + \beta) e^{i(k_0x+\alpha)} e^{i(\varphi_{2z}-\varphi_1+\delta\varphi_{L1})}, \quad (\text{S16})$$

and $M_{0x(y)}$ are coupling constants that can be tuned through individual laser intensity. Similarly, the Raman coupling between $|0\rangle$ and $|-1\rangle$ can be written as

$$M_{2z,3x} = \sum_F \frac{\Omega_{2z,F,7/2}^* \Omega_{3x,F,5/2}}{\Delta_p} = M'_{0x} \cos(k_0x + \alpha) e^{i(k_0z+\beta)} e^{i(-\varphi_{2z}+\varphi_3)} \quad (\text{S17})$$

$$M_{2x,3z} = \sum_F \frac{\Omega_{2x,F,7/2}^* \Omega_{3z,F,5/2}}{\Delta_p} = M'_{0y} \cos(k_0z + \beta) e^{-i(k_0x+\alpha)} e^{i(-\varphi_{2x}+\varphi_3-\delta\varphi_{L3})}. \quad (\text{S18})$$

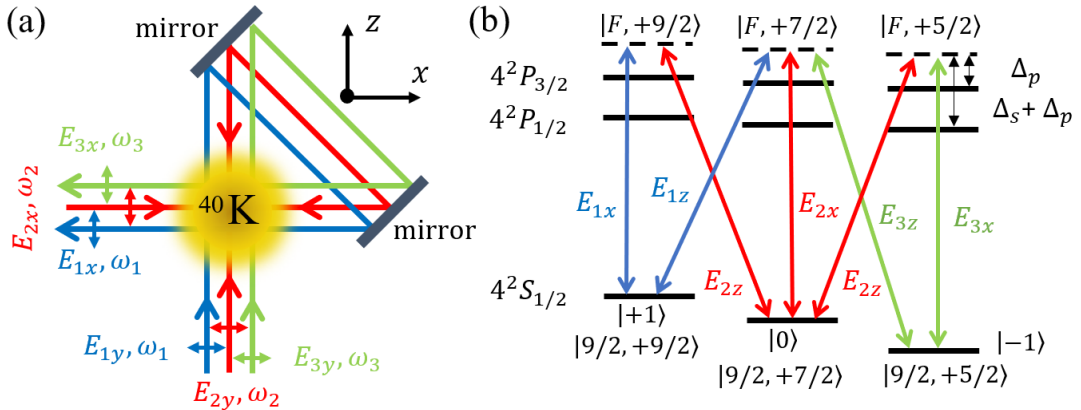


FIG. S3. (a) Experimental scheme for realizing spin-tensor-momentum coupling of rank-2 SHE in three-component fermionic ^{40}K atomic gases. The desired 2D SO coupling is realized through a standing wave $\mathbf{E}_{2x(z)}$ and two plane-wave $\mathbf{E}_{1(3)x(z)}$ laser fields. The arrows indicate the incident directions of the laser beams and each beam is reflected by two mirrors. (b) Level diagram and optical coupling in the hyperfine structure $|F, m\rangle$ of ^{40}K atoms. F is the quantum number of hyperfine states and Δ_s denotes fine-structure splitting.

We note that terms proportional to $\cos(k_0x + \alpha) \cos(k_0z + \beta)$ are antisymmetric to each lattice site in both x and y directions and thus can be neglected for low-band physics. The Raman coupling terms are further simplified as

$$\mathcal{M}_{+1,0} = (M_x - M_y \cos \delta\varphi_{L1}) - iM_y \sin \delta\varphi_{L1}, \quad (\text{S19})$$

$$\mathcal{M}_{0,-1} = (M'_x - M'_y \cos \delta\varphi_{L3}) + iM'_y \sin \delta\varphi_{L3}, \quad (\text{S20})$$

where $M_x = M_{0x} \cos(k_0x + \alpha) \sin(k_0z + \beta)$, $M_y = M_{0y} \cos(k_0z + \beta) \sin(k_0x + \alpha)$ and $M'_{x(y)}$ are defined similarly. In the above equations, we also choose the initial phase of the lasers so that $e^{i(\varphi_{2z} - \varphi_1)} = i$ and $e^{i(-\varphi_{2z} + \varphi_3)} = -i$. Since $|\omega_1 - \omega_3|/\omega_2 \ll 1$, we have $\delta\varphi_{L1} \approx \delta\varphi_{L3} = \delta\varphi_L$. Assuming the coupling constants are tuned to be equivalent $M'_x = M_x$ and $M'_y = M_y$, the total effective Hamiltonian becomes

$$H = \frac{\mathbf{p}^2}{2m} + V(\mathbf{r}) + \mathcal{M}_x(\lambda_1 + \lambda_6) + \mathcal{M}_y(\lambda_2 - \lambda_7) + \frac{\delta_T}{2} F_z^2 + \frac{\delta_V}{2} F_z, \quad (\text{S21})$$

where $\mathcal{M}_x = M_x - M_y \cos \delta\varphi_L$, $\mathcal{M}_y = M_y \sin \delta\varphi_L$ and the Zeeman terms are incorporated into the detunings in the ground-state manifold. When $\delta\varphi_L = \pi/2$, the spin-orbit coupling becomes $M_x(\lambda_1 + \lambda_6) + M_y(\lambda_2 - \lambda_7)$.

As we consider the lowest s -orbital $\phi_{s,\sigma}$ ($\sigma = +1, 0, -1$) and nearest-neighbor hopping, the spin-orbit coupling part of the tight-binding Hamiltonian can be written as

$$H_{\text{SOC}} = \sum_{\langle i,j \rangle} \left(t_{\text{so},+}^{ij} \hat{c}_{i,+1}^\dagger \hat{c}_{j,0} + h.c. + t_{\text{so},-}^{ij} \hat{c}_{i,0}^\dagger \hat{c}_{j,-1} + h.c. \right),$$

where hopping strengths can be expressed as overlap integrals

$$t_{\text{so},+}^{ij} = \int d^2\mathbf{r} \phi_{s,+1}^i(\mathbf{r}) [M_x(x,y)(\lambda_1 + \lambda_6) + M_y(x,y)(\lambda_2 - \lambda_7)] \phi_{s,0}^j(\mathbf{r}), \quad (\text{S22})$$

$$t_{\text{so},-}^{ij} = \int d^2\mathbf{r} \phi_{s,0}^i(\mathbf{r}) [M_x(x,y)(\lambda_1 + \lambda_6) + M_y(x,y)(\lambda_2 - \lambda_7)] \phi_{s,-1}^j(\mathbf{r}). \quad (\text{S23})$$

Finally, the spin-orbit coupling in low-energy Bloch Hamiltonian reads $\lambda_{\text{SO}} k_x(\lambda_1 + \lambda_6) + \lambda_{\text{SO}} k_z(\lambda_2 - \lambda_7)$, $\lambda_{\text{SO}} = 2t_{\text{SO}}$, which realizes the desired spin-tensor-momentum coupling for rank-2 SHE discussed in main text.

S5: Rank-2 spin accumulation. In the rank-2 SHE, the counterflow of spin currents of $|0\rangle$ and $\frac{1}{2}|+1\rangle + \frac{1}{\sqrt{2}}|-1\rangle$ results in the rank-2 spin accumulation on the lateral edges of the sample, as illustrated in Fig. 1 of the main text. Now we consider cold atoms confined by a harmonic trap along the y direction that can be described by

$$H = \tilde{H}_{F=1} + \frac{1}{2}m\omega^2 y^2, \quad (\text{S24})$$

where $\tilde{H}_{F=1}$ encodes the spin-tensor-momentum coupling, as shown in Eq. (S6). Here we assume the harmonic trap along the x direction is very weak and can be neglected in our calculation (or a box potential along x direction is considered). Because the harmonic trap breaks the translational symmetry in the y direction, we separate the Hamiltonian into two parts $H = H_0 + H_1$ where

$$H_0 = -\frac{\hbar^2 \partial_y^2}{2m} + \frac{1}{2}m\omega^2 y^2 + \frac{\hbar^2 k_x^2}{2m} + \frac{\hbar^2 k_x k_0}{m} \lambda_5, \quad (\text{S25})$$

$$H_1 = -\frac{i\hbar^2 k_0 \partial_y}{m} \lambda_+,$$

with $k_0 = \lambda m/\hbar^2$. H_0 is just the quantum oscillator up to some constant terms. To simplify the notation, we set the oscillator length $l_\omega = \sqrt{\frac{\hbar}{m\omega}}$ as length unit and $\frac{1}{2}\hbar\omega$ as energy unit. Then Eq. (S25) becomes dimensionless as

$$H_0 = -\partial_\xi^2 + \xi^2 + l_\omega^2 k_x^2 + 2l_\omega^2 k_y k_0 \lambda_5, \quad (\text{S26})$$

$$H_1 = -2il_\omega k_0 \partial_\xi \lambda_+,$$

where $\xi = y/l_\omega$.

The eigenvalue of H_0 is

$$\varepsilon_{n,k_x,s} = (2n+1) + l_\omega^2 (k_x + sk_0)^2 - s^2 l_\omega^2 k_0^2 \quad (\text{S27})$$

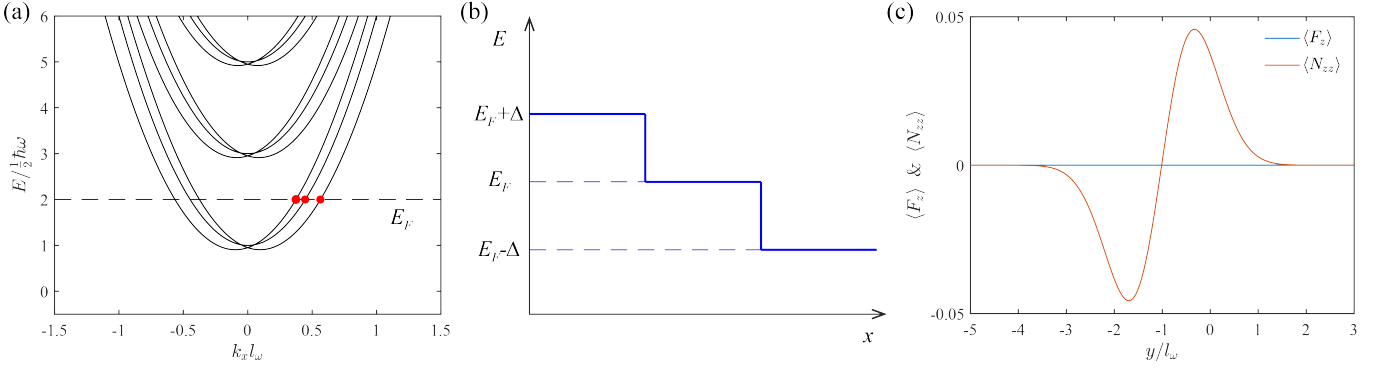


FIG. S4. (a) Energy spectrum of cold atoms with spin-tensor-momentum coupling and confined by a harmonic trap in the y direction. The blue dashed line denotes the Fermi energy. (b) Schematic step potential applied to drive cold atoms to move from left to right through the conducting channels in the middle which are highlighted by red dots in (a). (c) The distribution of rank-1 spin polarization $\langle F_z \rangle$ and rank-2 spin polarization $\langle N_{zz} \rangle$ in the middle region of (b) along the y direction. In the numerical simulation, we set $m = 0.2$, $\lambda = 0.5$, $\omega = 1$, and $\hbar = 1$.

and the corresponding wavefunction is

$$\psi_{n,k_x,s}(x,\xi) = e^{ik_x x} u_n(\xi) \chi_s, \quad u_n(\xi) = \frac{1}{\sqrt{2^n n! \sqrt{\pi}}} e^{-\xi^2/2} h_n(\xi). \quad (\text{S28})$$

where $h_n(\xi)$ is the Hermite polynomial. χ_s is the spin part of the wavefunction and the eigenstate of λ_5 , whose eigenvalues are $s = 0, \pm 1$. The wavefunction of the total Hamiltonian H can be expanded by $\psi_{n,k_x,s}(x,\xi)$ as

$$\Psi_{k_x}(x,\xi) = \sum_{n,s} c_{n,k_x,s} \psi_{n,k_x,s}(x,\xi), \quad (\text{S29})$$

and then $H\Psi_{k_x} = E_{k_x}\Psi_{k_x}$ yields the coupled equations

$$(\varepsilon_{n,k_x,+} - E_{k_y})c_{n,k_x,+} + i\sqrt{2(n+1)}l_\omega k_0 c_{n+1,k_x,-} - i\sqrt{2n}l_\omega k_0 c_{n-1,k_x,-} = 0, \quad (\text{S30})$$

$$(\varepsilon_{n,k_x,-} - E_{k_y})c_{n,k_x,-} + i\sqrt{2(n+1)}l_\omega k_0 c_{n+1,k_x,+} - i\sqrt{2n}l_\omega k_0 c_{n-1,k_x,+} = 0, \quad (\text{S31})$$

$$(\varepsilon_{n,k_x,0} - E_{k_y})c_{n,k_x,0} = 0. \quad (\text{S32})$$

Solving the three equations yields the energy spectrum of the system, as shown in Fig. S4(a), and the corresponding wavefunctions.

To detect the spin accumulation, we need to drive the cold atoms to flow along the x direction, that can be achieved by applying, for instance, a step potential (for the simplicity of the calculation), as shown in Fig. S4(b). In this configuration, the cold atoms move from the high potential on the left to the low potential on the right through the conducting channels in the middle region of Fig. S4(b). When the bias energy Δ is much smaller than $\hbar\omega$, the conducting channels are formed by states around the Fermi energy E_F , which are highlighted by red dots in Fig. S4(a). Then we calculate the distribution of rank-1 spin polarization $\langle F_z \rangle = \sum_{i=1}^3 \Psi_i^\dagger \hbar F_z \Psi_i$ and rank-2 spin polarization $\langle N_{zz} \rangle = \sum_{i=1}^3 \Psi_i^\dagger \hbar N_{zz} \Psi_i$ in the middle region, where $\Psi_{1,2,3}$ are the wavefunctions of the three states highlighted by red dots in Fig. S4(b). Apparently, there is a rank-2 spin accumulation, as shown in Fig. S4(c), while the rank-1 spin accumulation vanishes.

* These authors contributed equally to this work

† Email: chuanwei.zhang@utdallas.edu

[S1] Y. Kawaguchi and M. Ueda, Spinor Bose-Einstein condensates, *Phys. Rep.* **520**, 253 (2012).

[S2] G. Kimura, The Bloch vector for N-level systems, *Phys. Lett. A.* **314**, 339 (2003).

- [S3] Z. Wu et al., Realization of two-dimensional spin-orbit coupling for Bose-Einstein condensates, [Science](#) **354**, 83 (2016).
- [S4] L. H. Huang et al., Experimental realization of two-dimensional synthetic spin-orbit coupling in ultracold Fermi gases, [Nat. Phys.](#) **12**, 540 (2016).
- [S5] X.-J. Liu, K. T. Law, and T. K. Ng, Realization of 2D Spin-Orbit Interaction and Exotic Topological Orders in Cold Atoms, [Phys. Rev. Lett.](#) **112**, 086401 (2014).
- [S6] J. Hou, H. Hu, C. Zhang, Topological phases in pseudospin-1 Fermi gases with two-dimensional spin-orbit coupling, [Phys. Rev. B](#) **101**, 053613 (2020).